Architecture and permeability of post-cytokinesis plasmodesmata lacking cytoplasmic sleeves

William J. Nicolas[1], Magali S. Grison[1], Sylvain Trépout[2], Amélia Gaston[1,3], Mathieu Fouché[1,3], Fabrice P. Cordelières[4], Karl Oparka[5], Jens Tilsner[6,7], Lysiane Brocard [8]*, and Emmanuelle M. Bayer [1]*

1. Laboratory of Membrane Biogenesis, UMR5200 CNRS, University of Bordeaux, 71 Avenue Edouard Bourlaux, 33883 Villenave d'Ornon cedex, France
2. Institut Curie, Centre de Recherche, Bât. 112, Centre Universitaire, 91405 Orsay Cedex, France
3. Present address: UMR 1332 BFP, INRA, Univ. Bordeaux, Villenave d'Ornon 33140, France
4. Bordeaux Imaging Centre, UMS 3420 CNRS, CNRS-INSERM-University of Bordeaux 146, rue Léo Saignat, 33076 Bordeaux
5. Institute of Molecular Plant Sciences, University of Edinburgh, Edinburgh EH9 3BF, United Kingdom
6. Biomedical Sciences Research Complex, University of St Andrews, Fife KY16 9ST, United Kingdom
7. Cell and Molecular Sciences, The James Hutton Institute, Dundee DD2 5DA, United Kingdom
8. Bordeaux Imaging Centre, Plant Imaging Plateform, UMS 3420, INRA-CNRS-INSERM-University of Bordeaux, 71 Avenue Edouard Bourlaux, 33883 Villenave-d'Ornon Cedex, France

* Correspondence should be addressed to:
emmanuelle.bayer@u-bordeaux.fr; Phone: +33 (0) 55712 2539
lbrocard@bordeaux.inra.fr; Phone ++33 (0) 55712 2551

Running title: plasmodesmata structure by electron tomography

ABSTRACT

Plasmodesmata are remarkable cellular machines responsible for the controlled exchange of proteins, small RNAs and signalling molecules between cells. They are lined by the plasma membrane (PM), contain a strand of tubular endoplasmic reticulum (ER), and the space between these two membranes is thought to control plasmodesmata permeability.

Here, we have reconstructed plasmodesmata 3D ultrastructure with an unprecedented level of 3D information using electron tomography. We show that within plasmodesmata, ER-PM contact sites undergo substantial remodelling events during cell differentiation. Instead of being open pores, post-cytokinesis plasmodesmata present such intimate ER-PM contact along the entire length of the pores, that no inter-membrane gap is visible. Later on, during cell expansion, the plasmodesmata pore widens and the two membranes separate, leaving a cytosolic sleeve spanned by tethers whose presence correlates with the appearance of the intermembrane gap. Surprisingly, the post-cytokinesis plasmodesmata allow diffusion of macromolecules despite the apparent lack of an open cytoplasmic sleeve, forcing the reassessment of the mechanisms that control plant cell-cell communication.

INTRODUCTION

Plasmodesmata are membrane-lined channels that cross the plant cell wall and allow the exchange of molecules between virtually all plant cells. Plasmodesmata are required for coordinated plant growth and development, plant defence signalling[1–11] and are also exploited by viruses to spread from cell-to-cell and systemically throughout the plant[12,13].

Plasmodesmata are characterised by the apposition of two membranes: the plasma-membrane (PM) which lines the plasmodesmal pore and a strand of tubular endoplasmic reticulum (ER), which is tightly constricted into a rod-like structure known as the desmotubule[14–16]. These two plasmodesmal membrane compartments are highly specialised and contain specific sets of proteins and lipids, both of which are critical for proper function[7,8,17–22]. Inherent to their structure, plasmodesmata constitute a specialised type of membrane contact site (MCS), a general term describing areas of close (10-30 nm) apposition between two membranes[23–25]. In yeast and human cells MCS are well established sites for inter-organelle signalling, non-vesicular lipid exchange and calcium homeostasis[26–29]. In plasmodesmata, the function of ER-PM contacts remains an enigma[30] and signalling between the two membranes is still speculative. In current models however, the gap between the two membranes, the cytoplasmic sleeve, defines the space available for molecular trafficking, governing the size exclusion limit (SEL) of the pores. Plasmodesmata symplastic connectivity is strongly regulated in space and time. Their SEL can be modulated in response to biotic/abiotic stresses but also varies depending on the cell type and stage of tissue differentiation[7–9,31–36]. In any cases, the structural plasticity of plasmodesmata is assumed to be critical to adjust symplastic connectivity through the regulation of ER-PM spacing[2,36,37]. However, how plasmodesmata channels are built and organised within the narrow space between the ER and the PM, and how ER-PM spacing affects cell-to-cell connectivity remains little understood. While spectacular advances have been made over the last decade in imaging supramolecular structures such as the nuclear pore complex[38], we currently have no data on the 3D structure of plasmodesmata in higher plants. Past studies have greatly contributed to models of plasmodesmata ultrastructure[14,39,40] but they were based on 2D transmission electron micrographs where no depth (z-axis) and no information on the true 3D organisation of membrane

contacts within plasmodesmata was available. Yet, in depth understanding of plasmodesmata architecture and how it relates to intercellular connectivity is critical to understand their mechanisms of action.

Here we used electron tomography to gain access to the ultrastructure of plasmodesmata with an unprecedented level of 3D information and shed light on the structural plasticity of their ER-PM junctions. By acquiring multiple snapshots of plasmodesmata at different stages we reconstructed the structural dynamics of their architecture from their biogenesis to later maturation events. We unexpectedly show that within the plasmodesmal pores, ER-PM contacts undergo extensive remodelling, which varies from very tight contacts to intermembrane gaps of about 10 nm, spanned by spokes. Differences in ER-PM connections set apart two plasmodesmata morphotypes, which occurrence correlates with tissue growth and differentiation. Type II display archetypal organisation, with a cytoplasmic sleeve spanned by spoke-elements, and correspond to “mature” plasmodesmata. Contrary to the textbook model, we show that these “spokes” are insensitive to F-actin polymerization inhibitor drugs, suggesting they may not be related to the cytoskeleton. In addition to the archetypal plasmodesmata, we observed a second morphotype (Type I), which occurs in post-cytokinesis walls and unexpectedly presents such a tight contact between the ER and the PM that no visible intermembrane space remains. Despite the lack of visible cytoplasmic sleeve, these plasmodesmata are surprisingly capable of non-targeted movement of macromolecules such as GFP. Transition from Type I to Type II plasmodesmata is correlated with cell differentiation and tissue growth. Based on our data we propose that membrane-tethering elements control plasmodesmata MCS maturation and define different functional states of the plasmodesmata channels.

RESULTS

ER-PM spacing within plasmodesmata is regulated during tissue differentiation in root tips.

To analyse the ultrastructural organisation of plasmodesmata during tissue differentiation, we first focused on Arabidopsis root tip columella (COL), a tissue involved in gravitropism and soil excavation[41–43]. COL cells offered excellent plasmodesmata preservation after cryo-fixation and freeze-subtitution but also unequivocal traceability of cell lineage where plasmodesmata modification from early formation to later maturation stages can be easily traced. The columella is organised into several cell layers (Fig. 1a); the mitotically active COL cell initials (CCI), situated immediately below the root quiescent center (QC), which divide periclinally providing primary plasmodesmata on their division walls and supplying new COL cell layers[44] (identified as C1 for the inner-most layer, followed by C2, C3 etc. where the outer-most layer (CO) ultimately sloughs off[45]). Unlike the CCI, the COL cells from C1 to CO are unable to divide and undergo drastic cell elongation. This tissue therefore offers an excellent framework to track down potential modification in plasmodesmata architecture during cell differentiation.

Root tissues from one-week-old seedlings were high-pressure-frozen and freeze substituted to stay as close as possible to native conditions, then processed for electron tomography. The outermost cell layers of the COL (from C2 to C4) featured plasmodesmata with an archetypal ultrastructural organisation (n = 15; Fig. 1d). All presented a central desmotubule visible as an electron-opaque rod and an electron-lucent cytoplasmic sleeve spanned by multiple spoke-like tethers connecting the desmotubule to the PM (Fig. 1d, yellow arrows). These plasmodesmata had an average diameter (PM-PM; inner leaflets) of 39.3 ± 9.8 nm, while the desmotubule had a diameter of 19.15 ± 2.5 nm, and they traversed thick cell walls (Fig. 1e,f) and could display branched morphology (data not shown). On the opposite boundary, at the CCI interfaces, newly established plasmodesmata were of drastically different appearance. They presented a grainy electron dense interior with surprisingly no detailed internal features and no visible cytoplasmic sleeve (n = 20; Fig. 1b). They traversed the very thin CCI walls (79.1 ± 44.5 nm; Fig. 1e) and their average diameter (PM-PM; inner leaflets) was significantly smaller (23.2 ± 5.4 nm) than plasmodesmata encountered in

differentiated COL cells (Fig. 1f). Although not readily visible, nearly all plasmodesmata observed (n = 18 out of 20) presented cortical ER entering the pores in the form of an electron-dense rod suggesting that despite their tiny size they contained a desmotubule (Fig. 1b, black arrowheads). When comparing the size of the desmotubule in archetypal COL plasmodesmata, to the diameter of the CCI pores, we found no significant difference (Fig. 1f), suggesting that these non-canonical plasmodesmata presented an unconventional and underrated organisation with a very close ER-PM apposition within the entire length of the pores. For clarity, we called plasmodesmata with no visible cytoplasmic sleeve Type I (CCI) and Type II when both the ER-PM electron-lucent gap and the spoke elements were present (from C2 to C4). A transitional stage, between Type I and Type II, was visible at the C1 cell layer (Fig. 1c). While Type I plasmodesmata predominate at the CCI/C1 cell interface, the opposite transverse cell wall (the C1-C2 interface) displayed plasmodesmata with intermediate structural organisation and a partially "opened" cytoplasmic sleeve (n = 15). At this stage however, spoke-like tethers were difficult to distinguish.

Altogether our results indicate that ER-PM contacts within plasmodesmata may be differentially regulated during tissue differentiation in COL cells and reveal unexpected ultrastructural organisation of plasmodesmata in the CCI where no visible electron-lucent cytoplasmic sleeve remains between the two tightly apposed membranes.

Type II plasmodesmata membrane tethers control ER-PM gaps and are actin-independent.

The archetypal Type II plasmodesmata are characterised by the presence of spoke-like tethers that appeared as fine, electron-dense strands bridging the membranes across the cytoplasmic sleeve (Fig. 2a-c). In COL cells, the spokes were numerous and regularly spaced, with an average of 8 ± 3 nm (n= 8 plasmodesmata tomograms, 112 tethering elements measured) between the tethers and often the position of the tethers on opposite sides of the desmotubule matched up (Fig. 2a,b yellow arrow). Their length varied from 4 nm to 20 nm with a mean value of 9.7 ± 3.3 nm (Fig. 2d). Most tethers consisted of single, unbranched filaments, but V- and Y-shaped tethers were occasionally observed, in which case the two branches could either connect to the PM or to the desmotubule (Fig. 2e). Spokes of similar appearance and

length were also observed in Arabidopsis cultured cell plasmodesmata (Fig.2d; see also Fig. 3b).

The spoke appearance was concomitant with the transition from Type I to Type II, suggesting that these structures may be involved in controlling the spacing between the desmotubule and the PM. In root COL cells but also in Arabidopsis cultured cells, transitioning or Type II plasmodesmata sometimes presented subsections of the cytoplasmic sleeve gap devoid of spokes (Suppl. Fig. 1 and Fig. 3b) that seemed larger and looser when compared to cytoplasmic sleeve gaps spanned by spokes. To quantify this difference, we measured the cytoplasmic sleeve gaps in subsections of Type II pores harbouring cytoplasmic sleeve gaps spanned by or devoid of spoke-like tethers. The distance between the two membranes was maintained at around 9.6 ± 2.44 nm when the spokes were present whereas this distance nearly doubled, and was more variable, when the spokes were absent 18.38 ± 7.26 nm (Fig. 2f; see also similar results for cultured cells). Our data therefore suggests that there is a direct correlation between the presence of spoke-like tethers and the control of ER-PM spacing.

In conventional models of plasmodesmata, the spokes are often depicted as myosin molecules that would tether the two membranes by binding with F-actin imbedded in the desmotubule [46–51]. This model was built upon immunological data[52–54] and functional cell-to-cell communication tests[49,55]. If true, disturbing the delicate synthesis/degradation balance of F-actin homeostasis could affect plasmodesmata structure and more especially the spokes elements. In this regard, Arabidopsis roots were treated with drugs altering F-actin polymerization (Latrunculin B and Cytochalasin D) and processed for tomography. Efficiency of the treatments was checked using the actin markers fimbrin actin binding domain 2-green fluorescent protein (35S::GFP-fABD2-GFP)[56]. We also used the Golgi markers, N-acetylglucosamine1 (NAG1)[57] and the SNARE protein MEMBRIN12 (MEMB12)[58] to test their mobility after drug treatment as the cytosolic streaming of Golgi vesicles is known to heavily rely on the actin network[59] (Supplementary movie 2). Despite alteration of the actin filament network (Fig. 2g-i), the spokes were still observed spanning the cytoplasmic sleeve (Fig. 2j,k) and we saw no significant differences in the pore dimensions or in the length distribution of the spoke-elements (Fig. 2d,l).

We therefore concluded that the spokes may control ER-PM spacing within the plasmodesmata pores but their nature remains unclear. The fact that treatments with F-

actin polymerization inhibitors did not affect plasmodesmal ultrastructure suggests the spokes could be stable actin elements or not cytoskeleton related[15].

Post-cytokinesis plasmodesmata display very close appositions between the desmotubule and the PM

A surprising outcome of Type I plasmodesmata organisation in the root CCI was the absence of a visible cytoplasmic sleeve. These plasmodesmata were only present in the mitotically active CCI and transition to Type II occurred rapidly across a single cell interface. To get more information about these non-canonical plasmodesmata, we next turned to Arabidopsis liquid cultured cells which are actively dividing, contain primary plasmodesmata[60] (Suppl. Fig. 3) and do not undergo cell differentiation.

An initial survey revealed the presence of both Type I and II plasmodesmata (Fig. 3a-b). Similar to the CCI, Type I plasmodesmata had a grainy appearance as if the pores were filled with electron dense material throughout the entire channel, with no cytoplasmic sleeve visible nor apparent sub-elements (Fig. 3a). Close examination of tomograms revealed the presence of ER membranes entering the pores (15 out of 17), supporting the presence of a desmotubule (Fig. 3c, yellow arrow; Supplementary movie 4). Type II plasmodesmata in cultured cells displayed a visible cytoplasmic sleeve (Fig. 3b) but in contrast with COL plasmodesmata, it was only occasionally spanned by spoke-like elements, and often presented subsections with direct contact between the desmotubule and the PM (Suppl. Fig. 5; Supplementary movies 6-7). Similar to COL cells, Type I plasmodesmata also had a significantly smaller diameter than Type II (23 ± 2.6 nm versus 37 ± 7.2 nm, respectively) (Fig. 3d). They also displayed a remarkably constant diameter (PM-PM; inner leaflets) along their entire length, which never varied by more than 5 nm. This contrasted with Type II, whose diameter could range from 25 nm to more than 40 nm within a single channel (Fig. 3e). Altogether our data support the view that Type I plasmodesmata present a desmotubule tightly apposed against the PM along the entire length of the pores and that these non-canonical plasmodesmata are not unique to CCI cells.

We next investigated whether Type I and Type II plasmodesmata in cultured cells were in open or closed configurations, or whether these morphotypes corresponded to two populations with distinct internal features. In order to visualise dynamics of plasmodesmata ultrastructure during tissue growth, we screened Arabidopsis cultured

cells at four, six and thirteen days after sub-culturing. At four days old, when the cells were at the beginning of the linear growth phase, we observed a majority of plasmodesmata with "opaque" appearance (77% against 23%), similar to CCI plasmodesmata. With cell ageing, the relative proportion of Type I and Type II was reversed and the majority of the pores had apparent cytoplasmic sleeves (72% of Type II at six-day-old) (Fig.3 f-g). This transition happened relatively quickly, between days four and six of cell culture. Consistent with these data, quantitative analyses showed that Type I plasmodesmata were preferentially associated with thin (101 ± 48 nm), presumably newly formed cell walls, whereas Type II appeared in thicker (202 ± 78 nm), presumably older, cell walls (Fig. 3h).

Our data suggest that Type I and Type II plasmodesmata correspond to two distinct morphotypes whose appearance is not only correlated with tissue differentiation but also cell ageing and/or cell wall modification. Type I occur in post-cytokinesis plasmodesmata and display unconventional structural features characterised by intimate membrane contact between the desmotubule and the PM along the entire length of the channels.

ER-PM contacts are likely to be established during cell plate biogenesis and may lead to Type I plasmodesmata.

Our data suggest that newly formed plasmodesmata can exhibit very close ER-PM appositions but it is not clear whether such intimate membrane contacts arise during the pore formation or are established post-cytokinetically. We therefore captured plasmodesmata biogenesis events in meristematic epidermal root cells (Fig. 4). As reported in previous studies[61,62] the earliest traceable event of plasmodesmata formation corresponded to ER membranes perforating the cell plate during the planar fenestrated sheet stage (Fig. 4a-f). At this early stage, the gaps within the fenestrated membrane network were still large (57.3 ± 19.7 nm, n = 8) compared to plasmodesmata diameter and the traversing ER strands were non-constricted with apparent lumen (23.5 ± 4.8 nm, n = 8). However, regardless of the non-constricted appearance of the ER, intimate ER-PM contacts were already evident at this stage (Fig. 4d-f, red arrows). As the gaps within the fenestrated sheet became narrower, the ER bilayers appressed and tight ER-PM contacts on both sides of the ER were more prominent (Fig. 4g-l).

Our observations are consistent with an ER-PM attachment occurring in early stages of plasmodesmata biogenesis, before fenestrae closure and ER "entrapment".

Type I plasmodesmata with no visible cytoplasmic sleeve allows non-selective molecule diffusion.

Current models for cell-to-cell trafficking postulate that there is a direct link between ER-PM spacing and plasmodesmata permeability[2,36,37,49]. Surprisingly, our data revealed that newly formed plasmodesmata (Type I) are narrow with no apparent cytoplasmic sleeve. We therefore evaluated their permeability.

First, we focused on the CCI/C1 interface and used fluorescence recovery after photobleaching (FRAP) after loading the cells with carboxyfluorescein diacetate (CFDA), a membrane permeant fluorophore that is cleaved by intracellular esterases, yielding a membrane impermeant form of the probe[63] (Fig. 5a-c). We bleached a row of cells including the CCI (see Fig. 5a), the QC and adjacent lateral root cap cells to minimize recovery from lateral cells and isolate the CCI-C1 interface. After photobleaching we observed a fast recovery within the CCI suggesting that the probe was able to rapidly diffuse (half time recovery was of 9.7 seconds; n = 10), through the CCI/C1 interface, which contain only Type I plasmodesmata (Fig. 5c).

As CFDA has an estimated Stokes radius of only 0.61 nm[64], we next investigated the cell-to-cell diffusion of GFP, which has a Stokes radius of 2.82 nm[65]. To do so, we used Arabidopsis plants expressing GFP under the control of the phloem specific promoter SUC2[66]. In such lines, GFP expression driven by the SUC2 promoter serves as a marker for non-targeted macromolecular movement[9,11] as it is expressed in the phloem companion cells (Fig. 5d, green) and then diffuses in the neighbouring tissues when plasmodesmal permeability allows it. GFP fluorescence measurements show that GFP was able to diffuse into the root tip including the CCI cells that are exclusively surrounded by Type I plasmodesmata (Fig. 5e,f). Additionally, we measured a gradual decrease of fluorescence from the CCI to the outermost columella tiers (2 fold reduction; Fig. 5f), where only Type II plasmodesmata are found.

We could also observe that the transversal walls of root epidermal cells in the meristematic and division zone exclusively harboured Type I plasmodesmata (Fig.5g; n = 12). To confirm whether or not macromolecules can diffuse through Type I plasmodesmata, we used photo-activable GFP (35S::PA-GFP) and specifically activated

322 the GFP in one cell and monitored its spread in neighbouring cells. Within few minutes
323 cytoplasmic GFP fluorescence was apparent in neighbouring epidermal cells, indicating
324 symplastic movement across the apico-basal walls.
325 Our results demonstrate that although Type I plasmodesmata have no apparent
326 cytoplasmic sleeve, they can nevertheless allow cell-to-cell movement of
327 micromolecules and macromolecules.

DISCUSSION

The structural analysis of plasmodesmata channels is a formidable challenge given their nanoscopic size, location in the cell wall and dynamic nature. Using electron tomography of high pressure-frozen, near-native plasmodesmata, we resolved their ultrastructure at an unprecedented level of 3D detail. Our results revealed unforeseen architectural changes during cellular differentiation and tissue growth, with considerable modification in the internal organisation of these specialised membrane junctions. Based on our observation, we propose a model where archetypal plasmodesmata (Type II), harbouring a cytoplasmic sleeve and spoke-elements, derive from the unconventional Type I plasmodesmata established during cell plate formation. Contrarily to the archetypal model, Type I plasmodesmata present a remarkably close apposition between the desmotubule and the PM to such extent that no visible intermembrane space remains. Type I plasmodesmata we observed resemble, in their ultrastructure and size, pores previously reported in various species such as *N. tabaccum*, *A. pinnata* and *B. oleracea,* suggesting these may in fact be common structures[14,39,67]. Such proximity between membranes is uncommon amongst MCS structures, where the intermembrane spacing usually varies from 10 to 30 nm[23,25,68] and most likely membrane-bridging complexes are required to maintain this minimum gap[69]. Based on our measurements we propose that a ~2-3 nm wide electron-dense protein meshwork, associated with the desmotubule/PM interfaces, stabilises the contact and perhaps prevents the membranes from repelling each other as such an intimate membrane apposition is thermodynamically unstable[69]. Why are the two membranes in such close contact in Type I plasmodesmata remains to be elucidated. One possibility is that it could favour direct and rapid exchanges of molecules for the establishment of specialised membrane domains during early stages of plasmodesmata formation. We observed Type I plasmodesmata in young walls of Arabidopsis cultured cells, CCI and epidermal root cells, and we propose that these may actually be the predominant morphotype in young/meristematic tissues. As a matter of fact when going back to previous TEM reports on plasmodesmata structure, pores that resemble Type I plasmodesmata have been observed, very often in similar young, meristematic, sink tissues where walls are more likely to be newly divided[14,34,39,40,52,70,71]. Only later in cell development, the gap between the ER and the PM enlarges to form a cytoplasmic sleeve leading to the archetypal Type II plasmodesmata. As seen in the root, this “opening” of

the sleeve can occur quickly, on the opposite cell walls of a single cell. Our model depicts a desmotubule detaching from the PM, first in limited areas and then along the entire length of the channel. In advanced stages of plasmodesmata maturation, the desmotubule is centrally positioned and spokes are numerous and regularly spaced. These correspond to the canonical model of plasmodesmata ultrastructural organisation and have been observed many times in previous TEM studies although not with that level of detail[14,36,39,40,72,73].

A great variety of MCS exist in yeast, animal and plant cells, many of which have been shown to be controlled by tethering proteins or protein complexes[74] that can appear as electron-dense filament on electron micrographs[68]. These tethering elements physically and functionally connect the two opposing membranes. Tether-like structures are clearly visible in Type II plasmodesmata in the form of spoke-like elements, of about 9 nm in length, contacting the desmotubule and the PM. Their appearance coincides with the opening of the cytoplasmic sleeve and the adjustment of the intermembrane gap. This indicates the plasmodesmata tethers/spokes are likely to control ER-to-PM spacing throughout the pore maturation. At this stage it is not clear whether these spokes are already present at early stages of plasmodesmata formation, then unfolded. These plasmodesmata spokes have been observed before by classic TEM and have been thought to be F-actin-associated proteins such as myosin VIII[46–54]. However, our data suggest that membrane tethering at Type II plasmodesmata is not sensitive to destabilization by F-actin polymerization inhibitor drugs. We nevertheless cannot completely rule out that actin in plasmodesmata is unattainable by the drugs. Latrunculin B and Cytochalasin D are 0.4 and 0.5 kDa respectively and most certainly pass through plasmodesmata as compounds with similar molecular weights, such as carboxyfluorescein, do[75]. This suggests that the drugs can indeed physically pass through the pores and reach putative F-actin. However, plasmodesmata may contain very stable actin-associated structures that are not affected by the inhibitors of actin polymerization in our experimental conditions. Nevertheless, our results corroborate the alternative model introduced in 2011 by Tilsner et al. [15] questioning the presence of F-actin within the plasmodesmal pores due to sterical constraints and conveying a model where spokes are cytoskeleton-independent molecules. In any case, the identity of these plasmodesmata MCS tethers currently remains unanswered.

Unexpectedly, our data revealed that narrow, newly formed Type I plasmodesmata with no apparent cytoplasmic sleeve nonetheless enable fast small molecule diffusion and even non-selective macromolecule trafficking between cells which appears counterintuitive based on their morphology. These results are however consistent with previous data showing that i) young and meristematic sink tissues with newly divided cell walls harbour plasmodesmata reminiscent of the Type I morphology[14,34,39,40,70,71,76], and ii) Such young,sink or meristematic tissues often display higher symplastic connectivity than more mature (source tissues), allowing for instance free GFP movement from cell-to-cell, whereas source tissues do not[34,35,66,77,78]. This raises the question of how macromolecules can move through Type I plasmodesmata with such tight cytoplasmic sleeves. Regardless of the answer, our work forces a re-consideration of how trafficking is achieved in newly formed Type I plasmodesmata.

Altogether, our findings show that ER–PM contacts within plasmodesmata are dynamic and differentially regulated during tissue development and populated by either different tethering molecules and/or different tether conformations at various stages of plasmodesmata maturation. From our data it is clear the PM and desmotubule are always in intimate connection within the pores either through very tight membrane contacts or through spoke-like tethering elements. Similar to other MCS, the function of ER-PM may primarily be the exchange of molecules between the two organelles[23,24,30], which would then affect plasmodesmata function. In this context, the strikingly different ER-PM connections in Type I and Type II plasmodesmata may have profound implications for intermembrane exchanges and the regulation of plant cell-cell communication.

MATERIAL & METHODS

Biological material and growth conditions

Six day-old *Arabidopsis* (*Columbia*) root tips were grown vertically under greenhouse conditions on solid medium composed of *Murashige and Skoog* (MS) medium including vitamins (2.15g/L), MES (0.5g/L) and plant-Agar (7g/L), pH 5.7. Growth conditions were set at 22°C in a greenhouse with a long day 16h photoperiod (100µE/m/s). *Arabidopsis* (*Landsberg erecta*) culture cells were cultivated as described in [22] under constant light (20µE/m/s) at 22°C. Cells were used for experimentation at various ages ranging from four to thirteen-day-old (always mentioned in experiments).

For the establishment of a growth curve 5 independent liquid cultures were grown in the same conditions. 2mL of culture was sampled every day and the fresh weight was monitored (without the growth medium).

Cryofixation and freeze-substitution

200µm deep and 1.5 mm wide copper platelets were rapidly filled with either fresh cultured cell clusters or sectioned seedling root tips (approximately 1 mm in length). These platelets are beforehand coated with 1% phophastidyl-choline, hexadecene and the bottom is covered with a 50 µm thick aclar disk. Additional BSA 20% was also added in the platelet as a cryoprotectant filler. The prepared platelets containing the samples were then frozen with an EMPACT1 high pressure freezer (*Leica*, Vienna, Austria). The platelets were then transferred at -90°C into an AFS 2 freeze-substitution machine (*Leica*, Vienna, Austria) and incubated into a cryosubstitution mix: glutaraldehyde 0.5%, osmium tetroxide 2%, uranyl acetate 0.1% and water 1% in pure acetone. The incubation is only carried out at very low temperature (-90°C) for 48h. Then a progressive raise of the temperature of 3°C/h is initiated until -50°C is reached. The cryofixation mix is then carefully and thoroughly removed by 3 consecutive pure acetone washes followed by 3 pure ethanol washes. This very low temperature staining procedure produces a fine membrane staining allowing an improved contrast and resolution, suitable for the observation of nanometric details in electron tomography. To improve embedding, the samples were then carefully removed from the copper platelets and consecutively incubated in HM20 *Lowicryl* resin (*Electron Microscopy Science, EMS*) solutions of increasing concentration (dilutions done in pure ethanol): 25% and 50% (2

hours each), 75% (overnight), 100% (twice for 2 hours) and a final 4 day incubation in HM20 100% under UV light. The two first days of incubation were done at -50°C then temperature was quickly risen up to +20°C for the last two days. The use of such an electron lucent resin allowed us to reduce electronic scattering (hence noise) caused by resin-electron interaction, thus improving the x, y, z resolution.

Electron microscopy acquisitions

Cylindrical moulds (*Leica*, Vienna, Austria) were used to produce the blocks primarily because they made the production of longitudinal root sections easier. Sections were collected with an *Ultracut* S (*Leica,* Vienna, Austria). The sections used ranged from 90 nm to 180 nm depending on the volume to acquire. To prevent grid bars from blocking the image, 2x1mm oval slot grids filmed with formvar and carbon coated (*Electron Microscopy Science, EMS*) were used for section collection. Prior to observation, the grids are coated on both sides with 5 nm gold fiducials (essentially old immunogold secondary antibodies at a dilution ranging from 1/20 to 1/100 or a 1:1 mixture of 0.5% BSA and 5 nm colloidal gold solution from *BBI solution EM-GC5*) for the subsequent alignment step.

Observations were carried out on a FEI TECNAI Spirit 120kV electron microscope equipped with a -70 to +70° tilting goniometer. A tomography optimised single tilt specimen holder (*Fichione instruments, model-2020*) was also used to improve the tilting range. The tilt series of longitudinal views of plasmodesmata were acquired at magnifications ranging from x30,000 to x56,000, with images taken each degree. The *batch mode* special feature of the FEI 3D-explore tomography software allowed us to designate objects of interests, which were then acquired *via* an automated tilt series data collection process. This technique improved the throughput of our electron tomography workflow allowing us to acquire up to 10 tilt series overnight.

Tomogram reconstruction

The raw 4k by 4k pixels tilt series collected need to be aligned before reconstruction. For this manner, two strategies were used : fiducial-less alignment with TomoJ, an ImageJ plug-in[79,80] and fiducial alignment with eTomo, a graphic interface allowing the use of the IMOD tilt series processing package Etomo (http://bio3d.colorado.edu/imod/). With Etomo, 20 to 30 fiducials in the field of view

were used to correctly align all images. Good tilt series usually yielded errors of ≈ 1.2 pixels and below. Aligned stacks were binned two times before reconstruction to make data handling easier. Reconstruction was performed either by using the weighed back-projection or the SIRT algorithm (15 to 20 iterations with default parameters) of Etomo or the OSART iterative algorithm of TomoJ (100 iterations, 0.01 as relaxation coefficient, update every 5 images). Optional 2D filtering of the aligned stack performed prior to reconstruction with the default parameters of Etomo (0.35 cut-off and 0.05 sigma role-off) efficiently filtered the highest frequencies, rendering less noisy tomograms when needed. This extra filtering step allowed the SIRT algorithm of Etomo to yield more contrasted tomograms.

Combination of tomograms in the case of dual-tilt axis tomography was performed using Etomo with default parameters. Both single tilt tomograms were generated as described above. The cell wall region was eventually excluded from the processing as it increased the correlation error scores because of its lack of electron-dense features necessary for the patch correlation step.

Image segmentation and tomogram analysis

Manual segmentation of tomograms was performed with 3dmod and allowed us to visualise and appreciate the organisation of the sub-elements in a 3D space. Additionally, an efficient way of segmenting structures was to accurately outline their main contours throughout the volume using the interpolation tool (*drawing tools* IMOD package developed by Andrew Noske) and then generate an isosurface of the structure.

Systematic measurements were taken on all relevant raw tomograms (without filters applied to minimize measurement errors), comprising width of the desmotubule, plasmodesmata channel, cell wall thickness at the pores, length of the spokes if visible etc. Pore width, cytoplasmic sleeve space and spoke length were measured relative to the inner leaflets of the PM (facing the symplasm). The desmotubule was always measured in sections where it was clearly distinguishable and at its largest. Inter-spoke spacing, shape of spokes were also accounted for in relevant tomograms where spokes were clearly distinguishable.

TEM plasmodesmata Type I and II screening method

For Fig. 3 panels h and g, fractions of Type I and type II plasmodesmata were assessed by TEM in order to raise statistically significant numbers. This was possible because Type I and Type II plasmodesmata could be discriminated by classic TEM (Suppl. Fig. 8). To avoid potential sampling artefacts, a stereology based approach inspired from the dissector method[81,82] was used. Two to three biological replicates were used for plasmodesmata screening in culture cells for each time point.

Counting was done on 90 nm serial sections. Preliminary measures showed that only 20% of the plasmodesmata spotted on a reference section *n* could be followed on the contiguous lookup section *n+1*, meaning that 80% of the plasmodesmata spotted on a single section were "resolved". The counting was therefore performed on sections *n* and *n+2* to avoid any kind of double counting therefore giving more weight to larger pores. Plasmodesmata were considered resolved when the PM bilayers were clearly distinguishable.

Drug treatment

10mM/DMSO stock solutions of actin destabilizing agents latrunculin B (*Calbiochem*, 1mg) and cytochalasin D (*Sigma-aldrich,* 1mg) were used at a working concentration of 50µm (dilution in liquid MS medium) for 1h30min. Controls contained diluted DMSO only.

Permeability measurements

FRAP/CFDA: Plasmodesmal permeability assessments were made using FRAP on six day-old Arabidopsis root tips co-stained with CFDA (50µg/mL) and Propidium iodide. Roots were incubated in an aqueous CFDA solution for 5 minutes, then successively washed out in 3 water baths and mounted with propidium iodide in water for imaging. Acquisitions were made on a Zeiss LSM 880 equipped with an Argon laser (excitation 488 nm) and a 40x apochromate 1.30 oil-objective. In order to optimize the frame rate, cropping of the scanned area was done very consciously by limiting the height of the scanned area as much as possible and enlarging it in order to decrease the scanning time (≈ 90 ms at max scanning speed) while having access to the background, and neighbouring cells relative to the photobleached region. To assess the permeability specifically at the CCI-C1 interface, the photobleaching region consisted in a rectangle

encompassing CCI, QC cells and the surrounding initial cells, while recovery was monitored in the CCI only. This allowed us to isolate and measure fluorescence recovery in a unidirectional fashion. The FRAP routine consisted in 10 images pre-bleach at 20% laser power and max scanning speed (reaching ≈ 90 ms per image), ten iterations of photobleaching with 100% of 488 nm laser where pixel dwell time was increased to a value of ≈ 1µs/pixel. ≈ 400 post-bleach images were then acquired in order to reach the stationary phase of the fluorescence recovery with the same parameters than the pre-bleach images. The recovery profiles were accounted for noise and then double normalized and set to full scale mode (pre-bleach is set to 1 and first image post-bleach is set to 0) as described by Kote Miura in his online *FRAP-teaching module* (EAMNET-FRAP module, https://www.embl.de). Plotting and curve fitting was done using GraphPad Prism (*GraphPad Software, Inc)*.

pSUC2::GFP root : Regions of interest of same dimensions were used to measure the fluorescence intensity in multiple regions of six day-old *pSUC2::GFP* roots (vasculature, CCI and C1-CO columella layers) using confocal microscopy. The fluorescence intensities were then normalized relative to the intensity measured in the root vasculature. Background noise was substracted using wild type roots. Co-staining with propidium iodide allowed an easy visualization of the cellular organization of the root tip, thus allowing precise fluorescence intensity measurements in the different cells of interest.

Photoactivation in the root epidermis using 35S::PA:GFP lines : Six days old *35S::PA:GFP* arabidopsis roots were imaged using a Zeiss LSM880 confocal laser scanning microscope with 63x oil lens. Propidium iodide was excited at 488nm with 10% of laser power and fluorescence collected at 590-650 nm. PA-GFP was activated at 405nm with 3% of laser power and fluorescence emission collected at 505-550 nm with 10% 488 nm laser power. Photoactivation was done in single epidermal cell of the meristematic zone, where type I plasmodesmata were observed on the transversal walls. Both GFP and propidium iodide fluorescence were acquired every five minutes during 25 minutes. Quantification was done using Zenblue 2012 (Zeiss) in the activated and neighbouring cells (proximal and proximal+1) to assess GFP diffusion through apico-basal walls. Fluorescence intensity in the different cells was expressed as a percentage of total fluorescence (activated, proximal, proximal+1).

Data availability

The data that support the findings of this study are available from the corresponding author upon request

BIBLIOGRAPHY

1. Stahl, Y. & Faulkner, C. Receptor complex mediated regulation of symplastic traffic. *Trends Plant Sci.* **21,** 450–459 (2016).
2. Otero, S., Helariutta, Y. & Benitez-alfonso, Y. Symplastic communication in organ formation and tissue patterning. *Curr. Opin. Plant Biol.* **29,** 21–28 (2016).
3. Benkovics, A. H. & Timmermans, M. C. P. Developmental patterning by gradients of mobile small RNAs. *Curr. Opin. Genet. Dev.* **27,** 83–91 (2014).
4. Vaddepalli, P. *et al.* The C2-domain protein QUIRKY and the receptor-like kinase STRUBBELIG localize to plasmodesmata and mediate tissue morphogenesis in Arabidopsis thaliana. *Dev* **141,** 4139–4148 (2014).
5. Daum, G., Medzihradszky, A., Suzaki, T. & Lohmann, J. U. A mechanistic framework for noncell autonomous stem cell induction in Arabidopsis. *Proc. Natl. Acad. Sci. U. S. A.* **111,** 14619–24 (2014).
6. Stahl, Y. *et al.* Moderation of arabidopsis root stemness by CLAVATA1 and ARABIDOPSIS CRINKLY4 receptor kinase complexes. *Curr. Biol.* **23,** 362–371 (2013).
7. Benitez-alfonso, Y. *et al.* Symplastic intercellular connectivity regulates lateral root patterning. *Dev. Cell* **26,** 136–47 (2013).
8. Faulkner, C. *et al.* LYM2-dependent chitin perception limits molecular flux via plasmodesmata. *Proc. Natl. Acad. Sci. U. S. A.* **110,** 9166–70 (2013).
9. Wu, S. *et al.* Symplastic signaling instructs cell division, cell expansion, and cell polarity in the ground tissue of Arabidopsis thaliana roots. *Proc. Natl. Acad. Sci.* (2016).
10. Lee, J.-Y. & Lu, H. Plasmodesmata: the battleground against intruders. *Trends Plant Sci.* **16,** 201–10 (2011).
11. Vatén, A. *et al.* Callose biosynthesis regulates symplastic trafficking during root development. *Dev. Cell* **21,** 1144–55 (2011).
12. Tilsner, J. *et al.* Replication and trafficking of a plant virus are coupled at the entrances of plasmodesmata. *J. Cell Biol.* **201,** 981–95 (2013).
13. Benitez-Alfonso, Y., Faulkner, C., Ritzenthaler, C. & Maule, A. J. Plasmodesmata: gateways to local and systemic virus infection. *Mol. Plant. Microbe. Interact.* **23,** 1403–12 (2010).
14. Ding, B., Turgeon, R. & Parthasarathy, M. V. Substructure of freeze-substituted

627 plasmodesmata. *Protoplasma* **169,** 28–41 (1992).
628 15. Tilsner, J., Amari, K. & Torrance, L. Plasmodesmata viewed as specialised
629 membrane adhesion sites. *Protoplasma* **248,** 39–60 (2011).
630 16. Knox, K. *et al.* Putting the squeeze on plasmodesmata: A role for RETICULONs in
631 primary plasmodesmata formation. *Plant Physiol.* **168,** 1563–72 (2015).
632 17. Salmon, M. S. & Bayer, E. M. F. Dissecting plasmodesmata molecular composition
633 by mass spectrometry-based proteomics. *Front. Plant Sci.* **3,** (2012).
634 18. Simpson, C., Thomas, C., Findlay, K., Bayer, E. & Maule, A. J. An Arabidopsis GPI-
635 anchor plasmodesmal neck protein with callose binding activity and potential to
636 regulate cell-to-cell trafficking. *Plant Cell* **21,** 581–94 (2009).
637 19. Thomas, C. L., Bayer, E. M., Ritzenthaler, C., Fernandez-Calvino, L. & Maule, A. J.
638 Specific targeting of a plasmodesmal protein affecting cell-to-cell communication.
639 *PLoS Biol.* **6,** (2008).
640 20. Fernandez-Calvino, L. *et al.* Arabidopsis plasmodesmal proteome. *PLoS One* **6,**
641 (2011).
642 21. Lee, J.-Y. *et al.* A plasmodesmata-localized protein mediates crosstalk between
643 cell-to-cell communication and innate immunity in Arabidopsis. *Plant Cell* **23,**
644 3353–73 (2011).
645 22. Grison, M. S. *et al.* Specific membrane lipid composition is important for
646 plasmodesmata function in Arabidopsis. *Plant Cell* **27,** 1–24 (2015).
647 23. Prinz, W. A. Bridging the gap: Membrane contact sites in signaling, metabolism,
648 and organelle dynamics. *J. Cell Biol.* **205,** 759–769 (2014).
649 24. Pérez-Sancho, J. *et al.* Stitching Organelles: Organization and Function of
650 Specialized Membrane Contact Sites in Plants. *Trends Cell Biol.* **26,** 705–717
651 (2016).
652 25. Gallo, A., Vannier, C. & Galli, T. Endoplasmic Reticulum–Plasma Membrane
653 Associations:Structures and Functions. *Annu. Rev. Cell Dev. Biol.* **32,** 279–301
654 (2016).
655 26. Filseck, J. M. Von *et al.* Phosphatidylserine transport by ORP/Osh proteins is
656 driven by phosphatidylinositol 4-phosphate. *Science* **349,** 432–36 (2015).
657 27. Chang, C. L. *et al.* Feedback regulation of receptor-induced ca2+ signaling
658 mediated by e-syt1 and nir2 at endoplasmic reticulum-plasma membrane
659 junctions. *Cell Rep.* **5,** 813–825 (2013).

28. Giordano, F. *et al.* PI(4,5)P2-Dependent and Ca2+-Regulated ER-PM interactions mediated by the extended synaptotagmins. *Cell* **153,** 1494–1509 (2013).
29. Chu, B.-B. *et al.* Cholesterol Transport through Lysosome-Peroxisome Membrane Contacts. *Cell* **161,** 291–306 (2015).
30. Tilsner, J., Nicolas, W., Rosado, A. & Bayer, E. M. Staying tight: plasmodesmata membrane contact sites and the control of cell-to-cell connectivity. *Annu. Rev. Plant Biol.* **67,** 23.1-23.28 (2016).
31. Gisel, A., Barella, S., Hempel, F. D. & Zambryski, P. C. Temporal and spatial regulation of symplastic trafficking during development in Arabidopsis thaliana apices. *Dev* **126,** 1879–1889 (1999).
32. Sivaguru, M. *et al.* Aluminum-induced 1,3-beta-D-glucan inhibits cell-to-cell trafficking of molecules through plasmodesmata. A new mechanism of aluminum toxicity in plants. *Plant Physiol.* **124,** 991–1006 (2000).
33. Li, W. *et al.* Callose deposition at plasmodesmata is a critical factor in restricting the cell-to-cell movement of Soybean mosaic virus. *Plant Cell Rep.* **31,** 905–16 (2012).
34. Oparka, K. J. *et al.* Simple, but not branched, plasmodesmata allow the nonspecific trafficking of proteins in developing Tobacco leaves. *Cell* **97,** 743–54 (1999).
35. Kim, I. & Zambryski, P. C. Cell-to-cell communication via plasmodesmata during Arabidopsis embryogenesis. *Curr. Opin. Plant Biol.* **8,** 593–9 (2005).
36. Schulz, A. Plasmodesmata widening accompanies the short-term increase in symplasmic phloem unloading in pea root tips under osmotic stress. *Protoplasma* **188,** 22–37 (1995).
37. Brunkard, J. O., Runkel, A. M. & Zambryski, P. C. The cytosol must flow: intercellular transport through plasmodesmata. *Curr. Opin. Cell Biol.* **35,** 13–20 (2015).
38. Beck, M. *et al.* Nuclear pore complex structure and dynamics revealed by cryoelectron tomography. *Science* **306,** 1387–90 (2004).
39. Overall, R. L., Wolfe, J. & Gunning, B. E. S. Intercellular communication in Azolla roots: I. Ultrastructure of plasmodesmata. *Protoplasma* **111,** 134–150 (1982).
40. Tilney, L. G., Cooke, T. J., Connelly, P. S. & Tilney, M. S. The structure of plasmodesmata as revealed by plasmolysis, detergent extraction, and protease digestion. *J. Cell Biol.* **112,** 739–47 (1991).

41. Moore, R., Fondren, W. M., Koon, E. C. & Wang, C. L. The influence of gravity on the formation of amyloplasts in columella cells of Zea mays L. *Plant Physiol.* **82,** 867–868 (1986).
42. Bennett, T. *et al.* SOMBRERO, BEARSKIN1, and BEARSKIN2 regulate root cap maturation in Arabidopsis. *Plant Cell* **22,** 640–654 (2010).
43. Staehelin, L. a, Zheng, H. Q., Yoder, T. L., Smith, J. D. & Todd, P. Columella cells revisited: novel structures, novel properties, and a novel gravisensing model. *Gravit. Space Biol. Bull.* **13,** 95–100 (2000).
44. Dolan, L. *et al.* Cellular-Organization of the Arabidopsis-Thaliana Root. *Dev* **119,** 71–84 (1993).
45. Hamamoto, L., Hawes, M. C. & Rost, T. L. The production and release of living root cap border cells is a function of root apical meristem type in dicotyledonous angiosperm plants. *Ann. Bot.* **97,** 917–923 (2006).
46. Overall, R. L. & Blackman, L. M. A model of the macromolecular structure of plasmodesmata. *Trends Plant Sci.* **1,** 307–311 (1996).
47. Oparka, K. J. Getting the message across: How do plant cells exchange macromolecular complexes? *Trends Plant Sci.* **9,** 33–41 (2004).
48. White, R. & Barton, D. The cytoskeleton in plasmodesmata: a role in intercellular transport? *J. Exp. Bot.* **62,** 5249–5266 (2011).
49. Radford, J. E. & White, R. G. Inhibitors of myosin, but not actin, alter transport through Tradescantia plasmodesmata. *Protoplasma* **248,** 205–16 (2011).
50. Mongrand, S., Stanislas, T., Bayer, E. M. F., Lherminier, J. & Simon-Plas, F. Membrane rafts in plant cells. *Trends Plant Sci.* **15,** 656–63 (2010).
51. Sevilem, I., Yadav, S. R. & Helariutta, Y. Plasmodesmata : Channels for intercellular signaling during plant growth and development. **1217,** 3–24 (2015).
52. White, R. G. *et al.* Actin associated with plasmodesmata. *Protoplasma* **180,** 169–184 (1994).
53. Radford, J. E. & White, R. G. Localization of a myosin-like protein to plasmodesmata. *Plant J.* **14,** 743–50 (1998).
54. Faulkner, C. R., Blackman, L. M., Collings, D. a, Cordwell, S. J. & Overall, R. L. Anti-tropomyosin antibodies co-localise with actin microfilaments and label plasmodesmata. *Eur. J. Cell Biol.* **88,** 357–69 (2009).
55. Ding, B., Kwon, M. & Warnberg, L. Evidence that actin filaments are involved in

controlling the permeability of plasmodesmata in Tobacco mesophyll. *Plant J.* **10,** 157–164 (1996).

56. Sheahan, M. B., Staiger, C. J., Rose, R. J. & McCurdy, D. W. A green fluorescent protein fusion to actin-binding domain 2 of Arabidopsis fimbrin highlights new features of a dynamic actin cytoskeleton in live plant cells. *Plant Physiol.* **136,** 3968–3978 (2004).

57. Boutté, Y. *et al.* Endocytosis restricts Arabidopsis KNOLLE syntaxin to the cell division plane during late cytokinesis. *EMBO J.* **29,** 546–58 (2010).

58. Marais, C. *et al.* The Qb-SNARE Memb11 interacts specifically with Arf1 in the Golgi apparatus of Arabidopsis thaliana. *J. Exp. Bot.* **66,** 6665–6678 (2015).

59. Bradley, M. O. Microfilaments and cytoplasmic streaming: Inhibition of streaming with cytochalasin. *J. Cell Sci.* **12,** 327–343 (1973).

60. Bayer, E., Thomas, C. L. & Maule, A. J. Plasmodesmata in Arabidopsis thaliana suspension cells. *Protoplasma* **223,** 93–102 (2004).

61. Hawes, C. R., Juniper, B. E. & Horne, J. C. Low and High voltage electron microscopy of mitosis and cytokinesis in maize roots. *Planta* **152,** 397–407 (1981).

62. Hepler, P. K. Endoplasmic reticulum in the formation of the cell plate and plasmodesmata. *Protoplasma* **111,** 121–133 (1982).

63. Rutschow, H. L., Baskin, T. I. & Kramer, E. M. Regulation of solute flux through plasmodesmata in the root meristem. *Plant Physiol.* **155,** 1817–26 (2011).

64. Wang, N. & Fisher, D. B. The Use of Fluorescent Tracers to Characterize the Post-Phloem Transport Pathway in Maternal Tissues of Developing Wheat Grains. *Plant Physiol.* **104,** 17–27 (1994).

65. Terry, B. R., Matthews, E. K. & Haseloff, J. Molecular characterization of recombinant green fluorescent protein by fluorescence correlation microscopy. *Biochem. Biophys. Res. Commun.* **217,** 21–27 (1995).

66. Imlau, A., Truernit, E. & Sauer, N. Cell-to-cell and long-distance trafficking of the green fluorescent protein in the phloem and symplastic unloading of the protein into sink tissues. *Plant Cell* **11,** 309–322 (1999).

67. Blackman, L. M., Harper, J. D. I. & Overall, R. L. Localization of a centrin-like protein to higher plant plasmodesmata. *Eur. J. Cell Biol.* **78,** 297–304 (1999).

68. Fernández-Busnadiego, R., Saheki, Y. & De Camilli, P. Three-dimensional architecture of extended synaptotagmin-mediated endoplasmic reticulum–plasma

membrane contact sites. *Proc. Natl. Acad. Sci.* **112,** (2015).
69. Li, F. *et al.* Energetics and dynamics of SNAREpin folding across lipid bilayers. *Nat. Struct. Mol. Biol.* **14,** 890–896 (2007).
70. Olesen, P. The neck constriction in plasmodesmata. *Planta* **358,** 349–358 (1979).
71. Burch-Smith, T. M. & Zambryski, P. C. Loss of increased size exclusion limit (ise)1 or ise2 increases the formation of secondary plasmodesmata. *Curr. Biol.* **20,** 989–993 (2010).
72. Bell, K. & Oparka, K. Imaging plasmodesmata. *Protoplasma* **248,** 9–25 (2011).
73. Robinson-Beers, K. & Evert, R. F. Ultrastructure of and plasmodesmatal frequency in mature leaves of sugarcane. *Planta* **184,** 291–306 (1991).
74. Eisenberg-Bord, M., Shai, N., Schuldiner, M. & Bohnert, M. A Tether Is a Tether is a Tether : Tethering at Membrane Contact Sites. *Dev. Cell* **39,** 395–409 (2016).
75. Duckett, C. M., Oparka, K. J., Prior, D. a M., Dolan, L. & Roberts, K. Dye-coupling in the root epidermis of Arabidopsis is progressively reduced during development. *Dev* **120,** 3247–3255 (1994).
76. Badelt, K., White, R. G., Overall, R. L. & Vesk, M. Ultrastructural Specializations of the Cell Wall Sleeve Around Plasmodesmata. *Am. J.* **81,** 1422–1427 (2016).
77. Kim, I., Kobayashi, K., Cho, E. & Zambryski, P. C. Subdomains for transport via plasmodesmata corresponding to the apical-basal axis are established during Arabidopsis embryogenesis. *Proc. Natl. Acad. Sci.* **102,** 11945–11950 (2005).
78. Kim, I., Cho, E., Crawford, K., Hempel, F. D. & Zambryski, P. C. Cell-to-cell movement of GFP during embryogenesis and early seedling development in Arabidopsis. *Proc. Natl. Acad. Sci. U. S. A.* **102,** 2227–2231 (2005).
79. Messaoudi, C., Boudier, T., Sanchez Sorzano, C. O. & Marco, S. TomoJ: tomography software for three-dimensional reconstruction in transmission electron microscopy. *BMC Bioinformatics* **8,** 288 (2007).
80. Sorzano, C. O. S. *et al.* Marker-free image registration of electron tomography tilt-series. *BMC Bioinformatics* **10,** 124 (2009).
81. Lucocq, J. Unbiased 3-D quantitation of ultrastructure in cell biology. *Trends Cell Biol.* **3,** 354–358 (1993).
82. Sterio, D. C. The unbiased estimation of number and sizes of arbitrary particles using the disector. *J. Microsc.* **134,** 127–136 (1984).

FIGURE LEGENDS

Figure 1. Plasmodesmata ER-PM contact site morphology evolves during tissue development in root tips.

(**a**) Schematic representation of Arabidopsis root tip cellular organisation, in which the colours depict cell lineage. Plasmodesmal ultrastructure was studied in the Columella tiers in light red (yellow boxes), from the C1 to C4 layer and in the COL cell initials in red (CCI, yellow asterisks). (**b-d**) Tomographic slices of representative plasmodesmata from the CCI (b), C1-C2 (c) and C3-C4 (d) interfaces, respectively 0.56, 0.56 and 0.49 nm thick, and their associated 3D segmentation highlighting the changes in ER-PM architecture within the pores during COL cell differentiation. In CCI, appressed ER is seen entering the plasmodesmal pores (black arrowheads) and fills the entire canal (b). With tissue differentiation the cytoplasmic sleeve becomes gradually visible as the gap between the desmotubule and PM expands and become populated by spoke-like tethers (d, yellow arrows). In the C1/C2 transition zone there is no clearly identifiable spoke-elements in the cytoplasmic sleeve, only amorphous material (c, red). (**e**) Difference in cell wall thickness in CCI, C1-C2 and C3-C4 cells (Dunn's multiple comparison test **** $P<0.0001$). n = 94 for CCI, n = 27 for C1-C2 and n = 79 for C3-C4. (**f**) Average diameter of plasmodesmata (PM-PM, inner leaflets) and desmotubules in CCI, C1-C2 and C3-C4 cells (Dunn's multiple comparison test, * $P<0.05$, *** $P<0.001$). n = 20, n = 15 and n = 15 plasmodesmata tomograms for CCI, C1-C2 and C3-C4, respectively. CCI: columella cell initials; CS: cytoplasmic sleeve; Dt: desmotubule; ER: endoplasmic reticulum; QC: quiescent centre; PM: plasma membrane.

Figure 2. The spoke-like tethering elements of Type II plasmodesmata correlate with ER-PM spacing and are not sensitive to F-actin polymerization inhibitor drugs

(**a-c**) 1.24 nm thick tomographic slices depicting the typical and regular arrangement of the spoke-like tethering elements (yellow arrows) in Type II plasmodesmata, in the root columella (C2-C4). (b) Close-up view of the plasmodesma squared in (a). (c) Manual segmentation of (b). (**d**) Density representation of the spoke length, measured in COL cells and cultured Arabidopsis cells (non-treated, Latrunculin B, LaB and Cytochalasin D, CytD treated for roots and non treated for cultured cells). In either condition, there is a

peak density for spokes of about 9 nm in length. (**e**) Three close-up views of V/Y shaped spokes (red arrowheads) oriented towards the PM (top; middle) and the desmotubule (bottom). Scale bars = 5 nm. (**f**) Plot representation of the cytoplasmic sleeve gaps (desmotubule – PM distance) measured in subsections of transitioning or Type II pores with or without spokes. Both in roots and cultured cells the presence of spokes stabilizes the width of the intermembrane gap and keeps it at an average of 9.6 ± 2.44 nm whereas without the spokes this gap is 18.38 ± 7.26 nm (Mann-Whitney two tailed test, **** P<0.0001) n = 31 and n = 65 measurements in cell and root plasmodesmata respectively. (**g-l**) Type II plasmodesmata in COL cells (C2-C4) are not altered by F-actin-polymerization inhibitor drugs. (**g-i**) Maximum projections of confocal stacks taken in columellas of *Arabidopsis* marker lines fimbrin actin binding domain 35S::GFP-fABD2-GFP. In control conditions (**g**), cells show a dense, reticulated actin network, while after 1h30 hour treatment with 50µM Cytochalasin D (CytD, **h**) or Latrunculin B (LaB, **i**), the F-actin network is heavily altered. (**j-k**) 0.56 nm thick tomographic slices of plasmodesmata acquired in the columella of CytD (**j**) and LaB (**k**)-treated roots, showing that the spokes are still present. (**l**) The diameter (PM-PM; innerleaflets) of the pores and the desmotubule width remain unchanged both treatment (Dunn's multiple comparison test, **** P<0.0001, *** P<0.001) n = 41 plasmodesmata tomograms for non-treated (NT) condition, n = 13 for LaB and n = 16 for CytD treated condition. Dt: desmotubule ; PM : plasma membrane.

Figure 3. Very tight ER-PM contact in post-cytokinesis plasmodesmata

(**a-b**) Consecutive tomographic slices, of respectively 1.24 nm and 0.49 nm in thickness, of a Type I plasmodesma (a) and Type II plasmodesma (b, spokes are indicated by yellow dashes) in Arabidopsis cultured cells. (**c**) Type I plasmodesmata are traversed by the ER which becomes appressed just before entering the pores (yellow arrows). Three 0.56 nm thick tomographic slices and the corresponding 3D segmentation. (**d**) Plasmodesmata diameter (PM-PM; inner leaflets) of Type I (23 ± 2.6 nm) and Type II (37 ± 7.2 nm), and the desmotubule measured in Type II plasmodesmata (17 ± 2.4 nm). n = 17 and 22 tomograms for Type I and Type II plasmodesmata, respectively, and n = 22 for desmotubule measurements (**** P< 0.0001 by Mann-Whitney test). (**e**) plasmodesmata width at different points along the pores in Type I and II. Measurements (PM-PM; inner leaflets) were taken at the extremities and largest part of the channels. Type I

plasmodesmata have a remarkably constant diameter compared to Type II. n = 17 and n = 22 tomograms for Type I and Type II plasmodesmata, respectively. (**f**) Growth curve of Arabidopsis liquid cultured cells. Black arrows indicate the cell culture ages used for this study (four-, six- and thirteen-day-old). (**g**) Quantification of the relative proportion of Type I and II plasmodesmata in Arabidopsis cultured cells at four, six and thirteen days (n = 111, 89 and 22 screened plasmodesmata for four, six and thirteen days old cells). (**h**) Average cell wall thickness in relation to plasmodesmata Type. In four-day-old cultured cells, Type I plasmodesmata are abundant in thin young cell walls whereas Type II plasmodesmata are preferentially associated with thicker, older walls. n = 69 and 28 for Type I and II plamodesmata, respectively (**** $P < 0.0001$ by Mann-Whitney test). For (g) and (f), plasmodesmata screening was done on 90 nm thick sections by TEM (see M&M for details). CS: cytoplasmic sleeve; Do: days of culture; Dt: desmotubule; ER: endoplasmic reticulum; PM: plasma membrane.

Figure 4. Very tight ER-PM contacts are established during cell plate formation.

(**a-f**) 0.46 nm thick tomographic slices, and the associated segmentation show non-appressed ER strands trapped by the fenestrated cell plate, establishing very tight contacts (d-f, red arrows and dashed line) at very early stages of plasmodesmata initiation. (**g-l**) 0.56 nm thick (g, h) and 0.36 nm thick **(j, k)** tomographic slices depicting the establishment of very tight ER-PM contacts occurring on one end of the forming plasmodesma (g-i, red arrows and dashed line) and along its entire length (j–l, red arrows and dashed line). CP: cell plate; ER: endoplasmic reticulum; PM: plasma membrane.

Figure 5. Molecular trafficking through Type I plasmodesmata

(**a-c**) Plasmodesmata permeability at the CCI/C1 interface monitored by FRAP and CDFA (a) Col. 0 root tip co-stained with CFDA and Propidium Iodide. Orange and blue (CCI) boxes indicate regions that were photobleached and where fluorescence intensity was monitored, respectively. (b) Representative kymograph of CCI region (blue box in *a*). *Fire* LUT was applied to enhance visualization of the photobleaching and recovery. (**c**) Mean recovery curve with error bars indicating standard deviation (3 independent experiments; 10 successful FRAPs in 10 individual roots), showing rapid recovery of

CFDA within the CCI. The one-phase exponential association curve fit (R^2 = 0.86) calculated a half-time recovery of 9.7 seconds, a K constant of 0.07 s^{-1} and a Ymax of 0.86 (**d-f**) Non-targeted diffusion of free GFP in the COL cells using pSUC2::GFP lines. (d) Cartoon of Arabidopsis pSUC2::GFP root. Green cells represent the companion cells where the GFP is expressed. The presence of GFP in other parts of the root is due to diffusion through plasmodesmata. Red and blue colours show cell interfaces harbouring Type I or Type II plasmodesmata, respectively. (e) Confocal slices through Col 0 (left panels) and pSUC2::GFP (right panels) root tips exhibiting GFP signal (green) in the columella. Close up view (yellow boxed regions in upper panels) in the meristematic region show the CCI contours in the propidium iodide channel (white stars in the two bottom panels) reveal the CCI cells, right below the periblem layer containing the quiescent centre. GFP signal is visible in the meristematic area of pSUC2::GFP lines, in contrast to the absence of fluorescence in the Col.0 root tip. (f) GFP fluorescent quantification in the pSUC2::GFP lines in CCI, and C1-C4 COL layers (background was subtracted against Col-0 roots). Intensities are normalized within a given root relative to the intensity in the vascular system (set to 1). (n = 15 pSUC2::GFP roots and n = 10 Col.0 roots in 3 independent experiments). Wilcoxon test was used to compare each cell type to the CCI cells. * P<0.05, ** P<0.01, *** P<0.001.

(**g-i**) Photoactivated (PA)-GFP diffusion through Type I plasmodesmata. (g) Two 0.56 nm thick tomographic slices of Type I plasmodesmata in transversal walls of epidermal cells in the root meristematic zone. (h) Confocal slices showing PA-GFP signal in photoactivated cell (t0; white asterisk) and reaching the neighbouring cells after t25 minutes. Right panel represents a color-coded cartoon. (i) Fluorescence was quantified in the photo-activated (blue) and the adjacent (*n* proximal, in red and *n+1* in green) cells. PA-GFP fluorescence in activated cells consistently showed a decrease of intensity over time whereas neighbouring cells (*n*, *n+1)* showed a concomitant increase in fluorescence. (n = 15 roots; 5 independent experiments). Two-tailed Wilcoxon test was used to compare the fluorescence intensity in a given cell over time. The subsequent times points after photoactivation were always tested with t0 as the reference, for a given cell. ** P<0.01. CCI: columella cell initial; CFDA: carboxyfluorescein diacetate; COL: columella; FRAP: Fluorescence recovery after photobleaching; LUT: look up table.

Supplementary Fig 1.

(**a, b**) 0.56 nm thick tomographic slices of plasmodesmata found in the longitudinal cell walls of the C2 cell tier showing transition in their architecture between Type I and Type I with spoke-less central cavities. (**c**) 0.56 nm thick tomographic slices of a transitioning plasmodesmata at the C2-C3 layers interface. Spokes are starting to appear (white arrowheads) between PM and desmotubule and the cytoplasmic gap is consequently tighter than when spokes are absent. (**d**) Schematic representation depicting how the measurements were done for figure panel 3f. Measurements were always taken where the width of the gap was at its maximum. Blue double-headed arrow shows a typical measurement done in a spoke-less cavity contributing to the data plotted in panel 3f. Red double headed arrow shows same measurement executed in a cavity spanned by spoke-like tethers. Brown : cell wall ;Green : ER and the derived desmotubule ;Orange : spoke-like tethers.

Supplementary movie 2.

Timelapse of Mb12:YFP lines (a-c) and Ng1:GFP lines (d-f) taken at t = 0, 30min and 1h of treatment at 1 image every 5 seconds. Before treatment (a,d) golgi vesicles are numerous small and rapidely moving within the cells. After LaB (b, e) and CytD (c, f) treatment the vesicles were less mobile and tended to aggregate. The decrease in specific signal over time is due to photobleaching. All images were taken at same magnification under same conditions.

Supplementary Fig 3.

Cultured cells consist of small cell clusters and mostly contain primary plasmodesmata on contact walls that are formed during cytokinesis [60,62].

(a) Overview of Arabidopsis cell clusters in transmitted light. (b) 90 nm ultrathin section containing cells on a copper EM hexagonal grid. (c) TEM micrograph of a single stranded plasmodesma (white arrow) inserted in a division wall.

Supplementary movie 4.

A plasmodesma with Type I structure in Arabidopsis cultured cells.

The movie displays 0.68 nm thick tomographic slices and a 3D rendering of the data shown in Fig. 3c. ER/desmotubule in pale blue and PM in orange. Scale bar = 50 nm

Supplementary Fig 5.

(**a-d**) Tomograms of two Type II plasmodesmata from Arabidopsis cultured cells illustrating the fluctuation in the desmotubule to PM gap along the channels and points of very close ER-PM appositions (black arrowheads). The presence of spoke-elements are indicated by yellow arrows. Tomographic slices of 0.56 nm (a) and 0.46 nm (c) in thickness, and their corresponding segmentation (b and d). CS: cytoplasmic sleeve; Dt: desmotubule; ER: endoplasmic reticulum; PM: plasma membrane.

Supplementary movie 6&7.

Plasmodesma Type II in Arabidopsis cultured cells.

The movies display 0.56 nm thick tomographic slices and a manual segmentation of the data shown in Supplementary Fig.4. ER/desmotubule in pale blue, PM in orange and tethering elements in red.

Supplementary Fig 8.

Classic TEM micrographies of representative Type I (a, b) and Type II (c, d) plasmodesmata in gray levels and fake *Fire* coloring to highlight the presence or absence of cytoplasmic sleeve.

Acknowledgements

This work was supported by the grants by the Region Aquitaine (to E.M.B) and PEPS (Initial Support for Exploratory Projects to E.M.B) and National Agency for Research (Grant ANR-14-CE19-0006-01 to E.M.B). Electron and fluorescence microscopy analyses were performed at the Bordeaux Imaging Centre (http://www.bic.ubordeaux2.fr). The Region Aquitaine also supported the acquisition of the electron microscope (grant n°2011 13 04 007 PFM). We thank Yoselin Benitez-Alfonso for providing the Arabidopsis PA-GFP lines and Sébastien Mongrand, Vincent Arondel, Yohann Boutté, Yvon Jaillais and Chris Hawes for critical review of the article prior to submission.

Author contributions

Electron microscopy and associated-quantitative analyses were done by W.J.N. with the help of S.T. and L.B.. M.S.G. performed the cell-to-cell connectivity essays with the help of W.J.N and L.B. F.P.C. and L.B. provided technical support for the FRAP experiments and with image quantification and acquisition. All statistical analyses were run by W.J.N. and M.S.G. A.G. and M.F. performed the control tests for latrunculin and cytochalasin treatments in the roots. The manuscript was written by E.M.B. and W.J.N. with contributions of L.B., K.O. and J.T. Research was designed by E.M.B.

Additional information

Correspondence and requests for materials should be addressed to W.J.N and E.M.B.

Competing interests

The authors declare no competing financial interests.

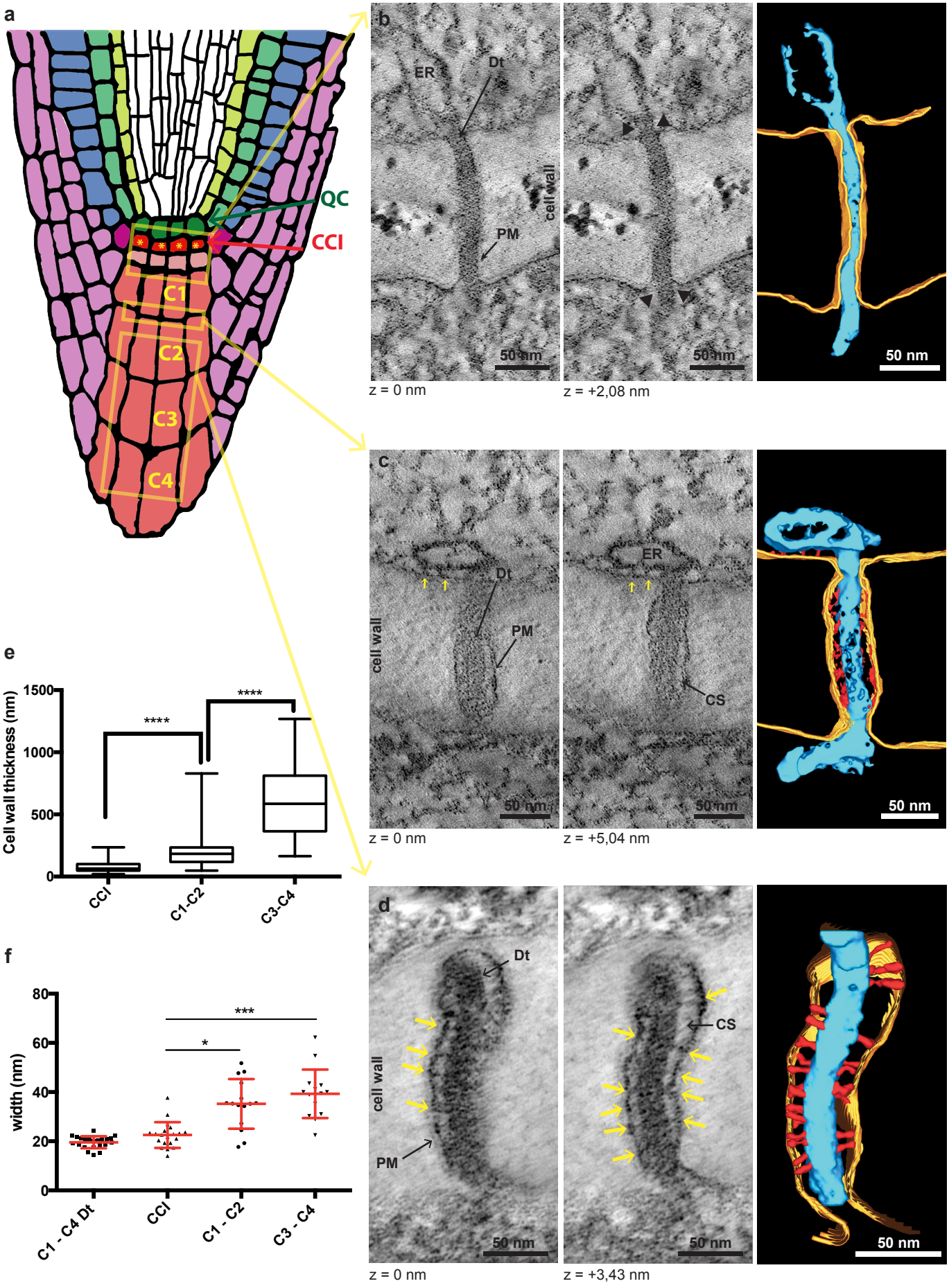
a
QC
CCI
C1
C2
C3
C4
b
ER
Dt
cell wall
PM
50 nm
z = 0 nm
z = +2,08 nm
c
Dt
PM
cell wall
ER
CS
50 nm
z = 0 nm
z = +5,04 nm
d
Dt
CS
cell wall
PM
50 nm
z = 0 nm
z = +3,43 nm
e
Cell wall thickness (nm)
1500
1000
500
0
****
****
CCI
C1-C2
C3-C4
f
width (nm)
80
60
40
20
0
***
*
C1 - C4 Dt
CCI
C1 - C2
C3 - C4

Figure 1. Plasmodesmata ER-PM contact site morphology evolves during tissue development in root tips.

(**a**) Schematic representation of Arabidopsis root tip cellular organisation, in which the colours depict cell lineage. Plasmodesmal ultrastructure was studied in the Columella tiers in light red (yellow boxes), from the C1 to C4 layer and in the COL cell initials in red (CCI, yellow asterisks). (**b-d**) Tomographic slices of representative plasmodesmata from the CCI (b), C1-C2 (c) and C3-C4 (d) interfaces, respectively 0.56, 0.56 and 0.49 nm thick, and their associated 3D segmentation highlighting the changes in ER-PM architecture within the pores during COL cell differentiation. In CCI, appressed ER is seen entering the plasmodesmal pores (black arrowheads) and fills the entire canal (b). With tissue differentiation the cytoplasmic sleeve becomes gradually visible as the gap between the desmotubule and PM expands and become populated by spoke-like tethers (d, yellow arrows). In the C1/C2 transition zone there is no clearly identifiable spoke-elements in the cytoplasmic sleeve, only amorphous material (c, red). (**e**) Difference in cell wall thickness in CCI, C1-C2 and C3-C4 cells (Dunn's multiple comparison test **** $P<0.0001$). n = 94 for CCI, n = 27 for C1-C2 and n = 79 for C3-C4. (**f**) Average diameter of plasmodesmata (PM-PM, inner leaflets) and desmotubules in CCI, C1-C2 and C3-C4 cells (Dunn's multiple comparison test, * $P<0.05$, *** $P<0.001$). n = 20, n = 15 and n = 15 plasmodesmata tomograms for CCI, C1-C2 and C3-C4, respectively. CCI: columella cell initials; CS: cytoplasmic sleeve; Dt: desmotubule; ER: endoplasmic reticulum; QC: quiescent centre; PM: plasma membrane.

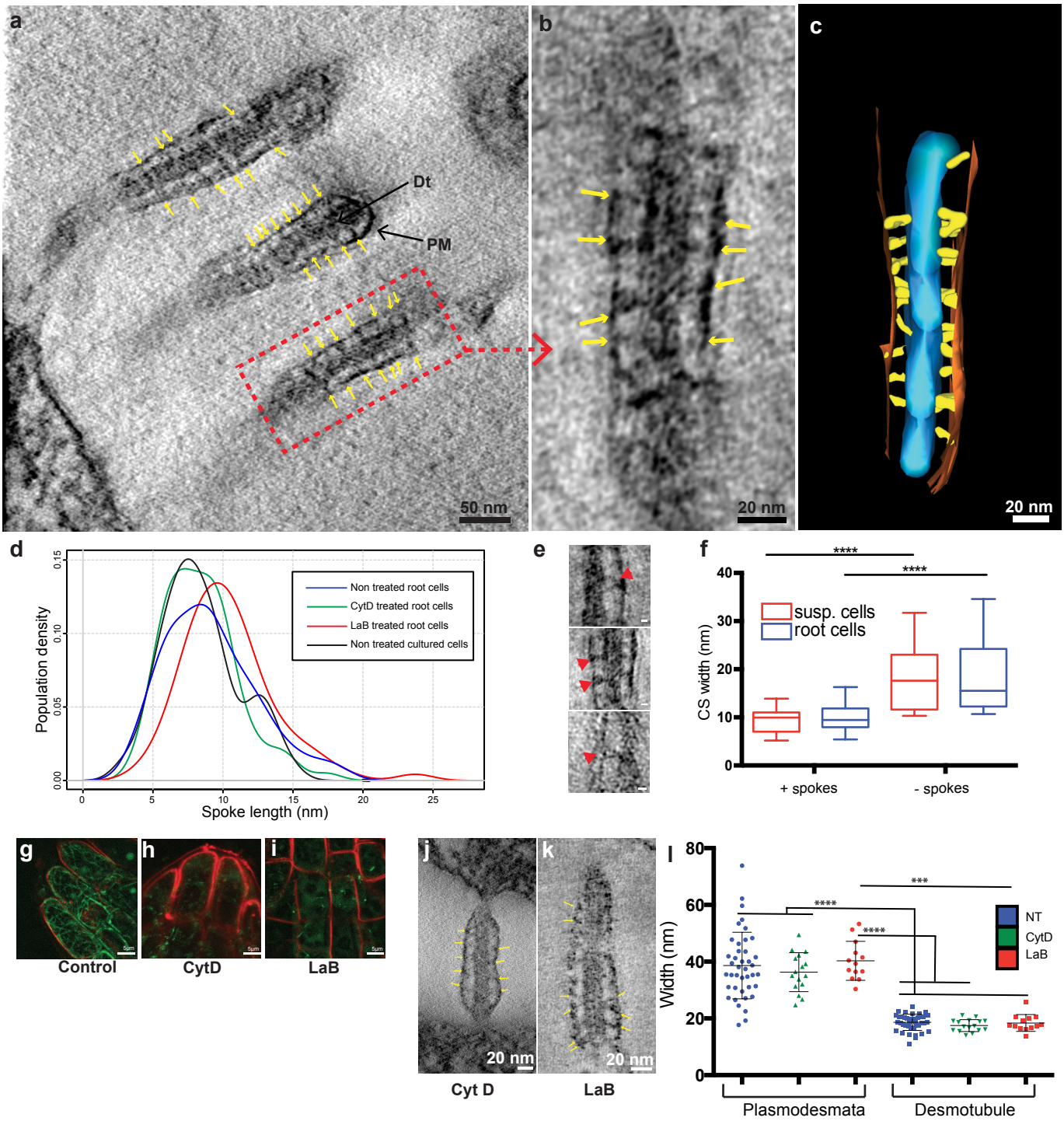
a
Dt
PM
50 nm
b
20 nm
c
20 nm
d
Population density
Spoke length (nm)
Non treated root cells
CytD treated root cells
LaB treated root cells
Non treated cultured cells
e
f
CS width (nm)
susp. cells
root cells
+ spokes
- spokes
****
****
g
h
i
Control
CytD
LaB
j
k
20 nm
20 nm
Cyt D
LaB
l
Width (nm)
NT
CytD
LaB
***
****
****
Plasmodesmata
Desmotubule

Figure 2. The spoke-like tethering elements of Type II plasmodesmata correlate with ER-PM spacing and are not sensitive to F-actin polymerization inhibitor drugs

(**a-c**) 1.24 nm thick tomographic slices depicting the typical and regular arrangement of the spoke-like tethering elements (yellow arrows) in Type II plasmodesmata, in the root columella (C2-C4). (b) Close-up view of the plasmodesma squared in (a). (c) Manual segmentation of (b). (**d**) Density representation of the spoke length, measured in COL cells and cultured Arabidopsis cells (non-treated, Latrunculin B, LaB and Cytochalasin D, CytD treated for roots and non treated for cultured cells). In either condition, there is a peak density for spokes of about 9 nm in length. (**e**) Three close-up views of V/Y shaped spokes (red arrowheads) oriented towards the PM (top; middle) and the desmotubule (bottom). Scale bars = 5 nm. (**f**) Plot representation of the cytoplasmic sleeve gaps (desmotubule – PM distance) measured in subsections of transitioning or Type II pores with or without spokes. Both in roots and cultured cells the presence of spokes stabilizes the width of the intermembrane gap and keeps it at an average of 9.6 ± 2.44 nm whereas without the spokes this gap is 18.38 ± 7.26 nm (Mann-Whitney two tailed test, **** $P<0.0001$) n = 31 and n = 65 measurements in cell and root plasmodesmata respectively.

(**g-l**) Type II plasmodesmata in COL cells (C2-C4) are not altered by F-actin-polymerization inhibitor drugs. (**g-i**) Maximum projections of confocal stacks taken in columellas of *Arabidopsis* marker lines fimbrin actin binding domain 35S::GFP-fABD2-GFP. In control conditions (**g**), cells show a dense, reticulated actin network, while after 1h30 hour treatment with 50µM Cytochalasin D (CytD, **h**) or Latrunculin B (LaB, **i**), the F-actin network is heavily altered. (**j-k**) 0.56 nm thick tomographic slices of plasmodesmata acquired in the columella of CytD (**j**) and LaB (**k**)-treated roots, showing that the spokes are still present. (**l**) The diameter (PM-PM; innerleaflets) of the pores and the desmotubule width remain unchanged both treatment (Dunn's multiple comparison test, **** $P<0.0001$, *** $P<0.001$) n = 41 plasmodesmata tomograms for non-treated (NT) condition, n = 13 for LaB and n = 16 for CytD treated condition. Dt: desmotubule ; PM : plasma membrane.

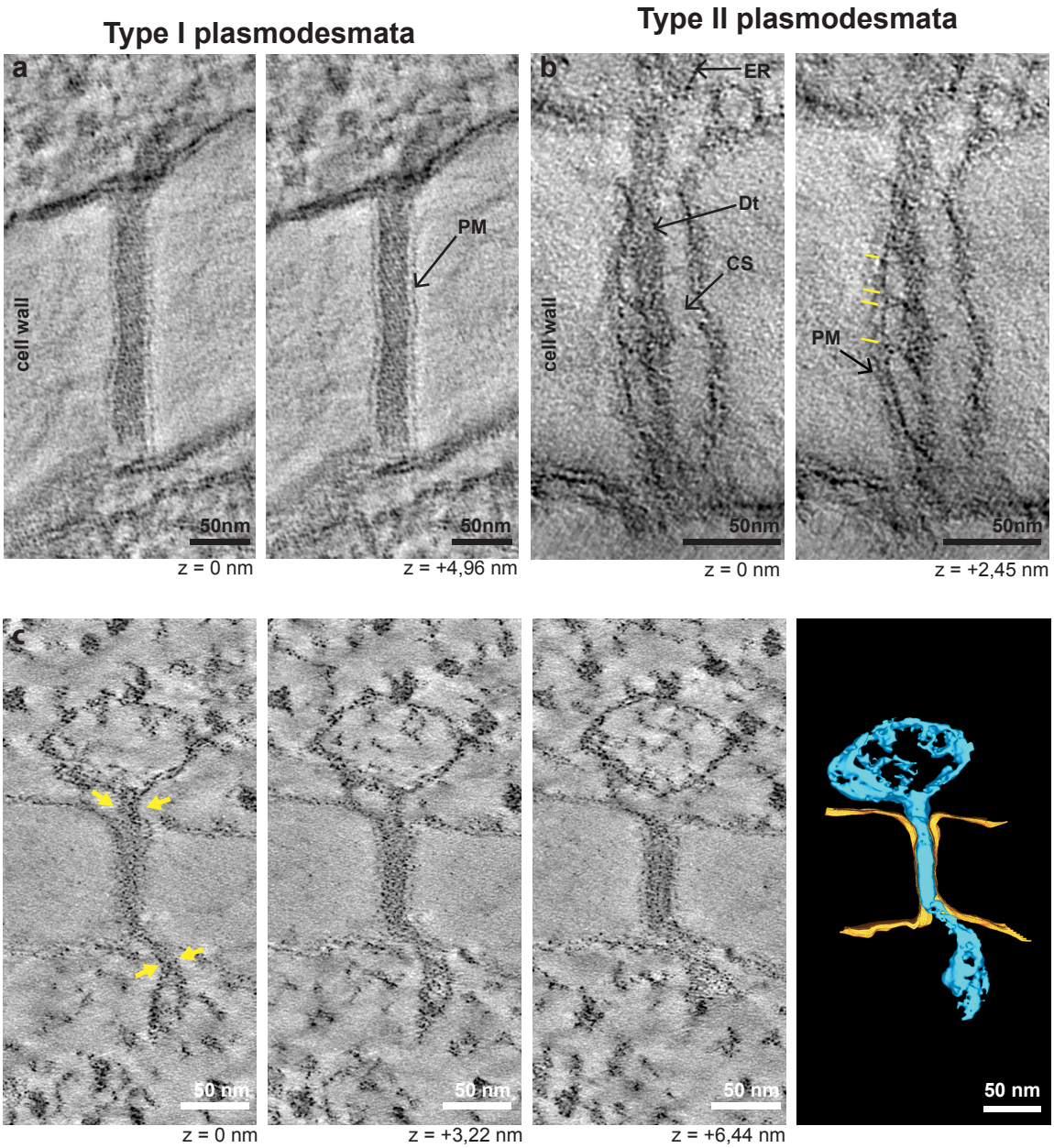
Type I plasmodesmata
Type II plasmodesmata
a
b
cell wall
PM
ER
Dt
CS
50nm
z = 0 nm
z = +4,96 nm
z = 0 nm
z = +2,45 nm
c
50 nm
z = 0 nm
z = +3,22 nm
z = +6,44 nm
d
****
Width (nm)
Type I
Type II
Desmotubule
e
Channel Width (nm)
Type I
Type II
Neck region
Widest region
Neck region
f
Fresh weight in mg (x 100)
Days of culture
g
Fraction (%)
Type I
Type II
4do
6do
13do
h
Cell wall thickness (nm)
Type I
Type II

Figure 3. Very tight ER-PM contact in post-cytokinesis plasmodesmata

(**a-b**) Consecutive tomographic slices, of respectively 1.24 nm and 0.49 nm in thickness, of a Type I plasmodesma (a) and Type II plasmodesma (b, spokes are indicated by yellow dashes) in Arabidopsis cultured cells. (**c**) Type I plasmodesmata are traversed by the ER which becomes appressed just before entering the pores (yellow arrows). Three 0.56 nm thick tomographic slices and the corresponding 3D segmentation. (**d**) Plasmodesmata diameter (PM-PM; inner leaflets) of Type I (23 ± 2.6 nm) and Type II (37 ± 7.2 nm), and the desmotubule measured in Type II plasmodesmata (17 ± 2.4 nm). n = 17 and 22 tomograms for Type I and Type II plasmodesmata, respectively, and n = 22 for desmotubule measurements (**** $P < 0.0001$ by Mann-Whitney test). (**e**) plasmodesmata width at different points along the pores in Type I and II. Measurements (PM-PM; inner leaflets) were taken at the extremities and largest part of the channels. Type I plasmodesmata have a remarkably constant diameter compared to Type II. n = 17 and n = 22 tomograms for Type I and Type II plasmodesmata, respectively. (**f**) Growth curve of Arabidopsis liquid cultured cells. Black arrows indicate the cell culture ages used for this study (four-, six- and thirteen-day-old). (**g**) Quantification of the relative proportion of Type I and II plasmodesmata in Arabidopsis cultured cells at four, six and thirteen days (n = 111, 89 and 22 screened plasmodesmata for four, six and thirteen days old cells). (**h**) Average cell wall thickness in relation to plasmodesmata Type. In four-day-old cultured cells, Type I plasmodesmata are abundant in thin young cell walls whereas Type II plasmodesmata are preferentially associated with thicker, older walls. n = 69 and 28 for Type I and II plamodesmata, respectively (**** $P < 0.0001$ by Mann-Whitney test). For (g) and (f), plasmodesmata screening was done on 90 nm thick sections by TEM (see M&M for details). CS: cytoplasmic sleeve; Do: days of culture; Dt: desmotubule; ER: endoplasmic reticulum; PM: plasma membrane.

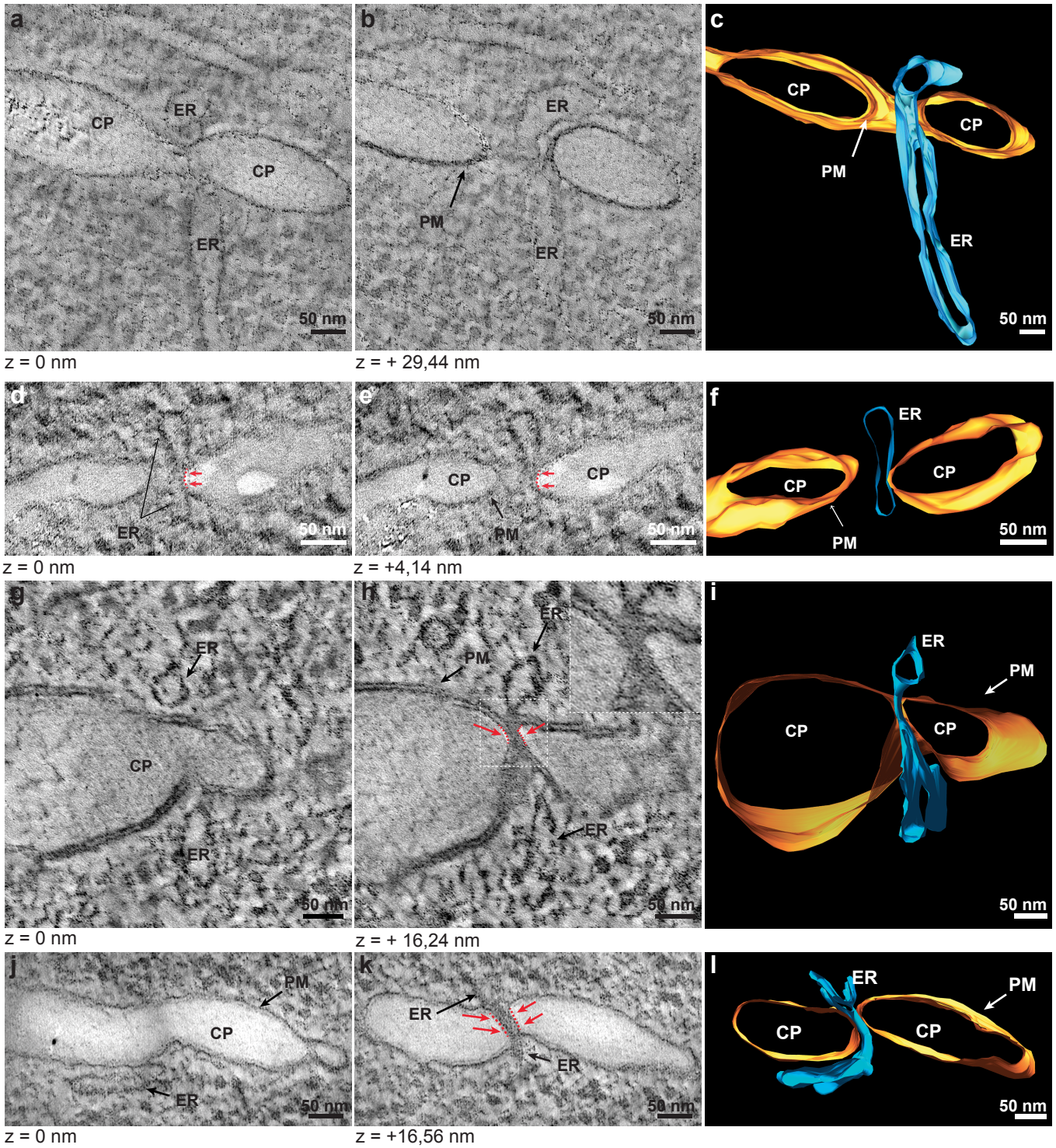
a
ER
CP
CP
ER
50 nm
z = 0 nm
b
ER
PM
ER
50 nm
z = + 29,44 nm
c
CP
CP
PM
ER
50 nm
d
ER
50 nm
z = 0 nm
e
CP
CP
PM
50 nm
z = +4,14 nm
f
ER
CP
CP
PM
50 nm
g
ER
CP
ER
50 nm
z = 0 nm
h
ER
PM
ER
50 nm
z = + 16,24 nm
i
ER
PM
CP
CP
50 nm
j
PM
CP
ER
50 nm
z = 0 nm
k
ER
ER
50 nm
z = +16,56 nm
l
ER
PM
CP
CP
50 nm

Figure 4. Very tight ER-PM contacts are established during cell plate formation. (**a-f**) 0.46 nm thick tomographic slices, and the associated segmentation show non-appressed ER strands trapped by the fenestrated cell plate, establishing very tight contacts (d-f, red arrows and dashed line) at very early stages of plasmodesmata initiation. (**g-l**) 0.56 nm thick (g, h) and 0.36 nm thick **(j, k)** tomographic slices depicting the establishment of very tight ER-PM contacts occurring on one end of the forming plasmodesma (g-i, red arrows and dashed line) and along its entire length (j–l, red arrows and dashed line). CP: cell plate; ER: endoplasmic reticulum; PM: plasma membrane.

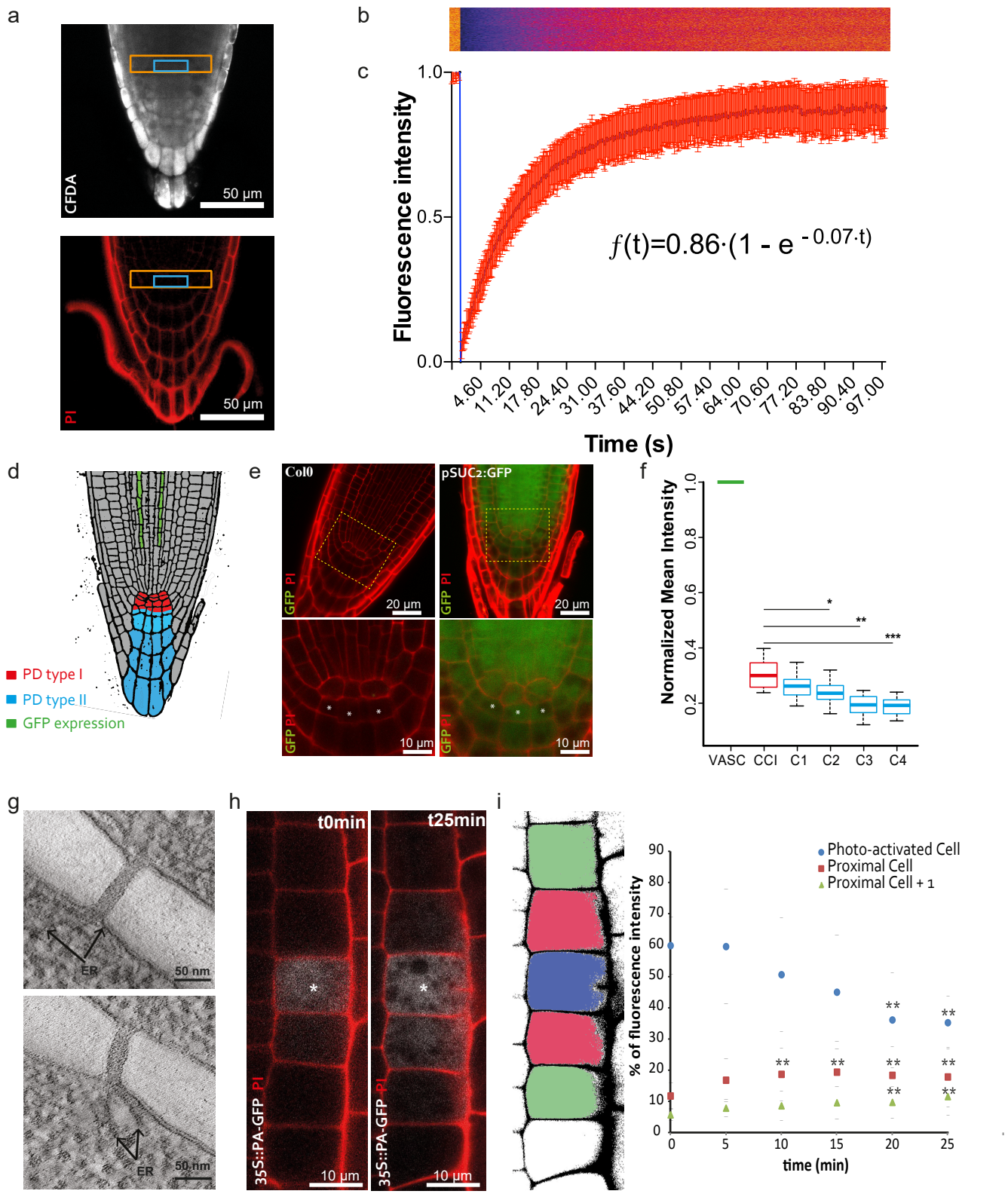
a
CFDA
50 µm
PI
50 µm
b
c
Fluorescence intensity
1.0
0.5
0.0
$f(t)=0.86\cdot(1 - e^{-0.07\cdot t})$
4.60
11.20
17.80
24.40
31.00
37.60
44.20
50.80
57.40
64.00
70.60
77.20
83.80
90.40
97.00
Time (s)
d
PD type I
PD type II
GFP expression
e
Col0
pSUC2:GFP
GFP PI
20 µm
10 µm
f
Normalized Mean Intensity
1.0
0.8
0.6
0.4
0.2
*
**
***
VASC
CCI
C1
C2
C3
C4
g
ER
50 nm
h
t0min
t25min
35S::PA-GFP PI
10 µm
i
% of fluorescence intensity
90
80
70
60
50
40
30
20
10
0
Photo-activated Cell
Proximal Cell
Proximal Cell + 1
0
5
10
15
20
25
time (min)

Figure 5. Molecular trafficking through Type I plasmodesmata

(**a-c**) Plasmodesmata permeability at the CCI/C1 interface monitored by FRAP and CDFA (a) Col. O root tip co-stained with CFDA and Propidium Iodide. Orange and blue (CCI) boxes indicate region that were photobleached and where fluorescence intensity was monitored, respectively. (b) Representative kymograph of CCI region (blue box in *a*). *Fire* LUT was applied to enhance visualization of the photobleaching and recovery. (**c**) Mean recovery curve with error bars indicating standard deviation (3 independent experiments; 10 successful FRAPs in 10 individual roots), showing rapid recovery of CFDA within the CCI. The one-phase exponential association curve fit (R^2 = 0.86) calculated a half-time recovery of 9.7 seconds, a K constant of 0.07 s^{-1} and a Ymax of 0.86

(**d-f**) Non-targeted diffusion of free GFP in the COL cells using pSUC2::GFP lines. (d) Cartoon of Arabidopsis pSUC2::GFP root. Green cells represent the companion cells where the GFP is expressed. The presence of GFP in other parts of the root is due to diffusion through plasmodesmata. Red and blue colours show cell interfaces harbouring Type I or Type II plasmodesmata, respectively. (e) Confocal slices through Col 0 (left panels) and pSUC2::GFP (right panels) root tips exhibiting GFP signal (green) in the columella. Close up view (yellow boxed regions in upper panels) in the meristematic region show the CCI contours in the propidium iodide channel (white stars in the two bottom panels) reveal the CCI cells, right below the periblem layer containing the quiescent centre. GFP signal is visible in the meristematic area of pSUC2::GFP lines, in contrast to the absence of fluorescence in the Col.0 root tip. (f) GFP fluorescent quantification in the pSUC2::GFP lines in CCI, and C1-C4 COL layers (background was subtracted against Col-0 roots). Intensities are normalized within a given root relative to the intensity in the vascular system (set to 1). (n = 15 pSUC2::GFP roots and n = 10 Col.0 roots in 3 independent experiments). Wilcoxon test was used to compare each cell type to the CCI cells. * P<0.05, ** P<0.01, *** P<0.001.

(**g-i**) Photoactivated (PA)-GFP diffusion through Type I plasmodesmata. (g) Two 0.56 nm thick tomographic slices of Type I plasmodesmata in transversal walls of epidermal cells in the root meristematic zone. (h) Confocal slices showing PA-GFP signal in photoactivated cell (t0; white asterisk) and reaching the neighbouring cells after t25 minutes. Right panel represents a color-coded cartoon. (i) Fluorescence was quantified in the photo-activated (blue) and the adjacent (*n* proximal, in red and *n+1* in green) cells. PA-GFP fluorescence in activated cells consistently showed a decrease of intensity over time whereas neighbouring cells (*n*, *n+1)* showed a concomitant increase in fluorescence. (n = 15 roots; 5 independent experiments). Two-tailed Wilcoxon test was used to compare the fluorescence intensity in a given cell over time. The subsequent times points after photoactivation were always tested with t0 as the reference, for a given cell. ** P<0.01. CCI: columella cell initial; CFDA: carboxyfluorescein diacetate; COL: columella; FRAP: Fluorescence recovery after photobleaching; LUT: look up table.